Lattice-Matched InGaAs–InAlAs Core–Shell Nanowires with Improved Luminescence and Photoresponse Properties

Julian Treu,*,[†,‡] Thomas Stettner,[†] Marc Watzinger,[⊥] Stefanie Morkötter,[†] Markus Döblinger,[∥] Sonja Matich,[†] Kai Saller,[†] Max Bichler,[†] Gerhard Abstreiter,[†,‡,§] Jonathan J. Finley,[†,‡] Julian Stangl,[⊥] and Gregor Koblmüller*,[†,‡]

[†]Walter Schottky Institut, Physik Department, and Center of Nanotechnology and Nanomaterials, Technische Universität München, Am Coulombwall 4, Garching, 85748, Germany

[‡]Nanosystems Initiative Munich (NIM), Schellingstrasse 4, München, 80799, Germany

[⊥]Institute of Semiconductor and Solid State Physics, Johannes Kepler University Linz, Altenbergerstrasse 69, Linz, 4040, Austria

[∥]Deparment of Chemistry, Ludwig-Maximilian Universität München, Butenandtstrasse 5-13, München, 81377, Germany

[§]Institute for Advanced Study, Technische Universität München, Lichtenbergstraße 2a, Garching, 85748, Germany

S *Supporting Information*
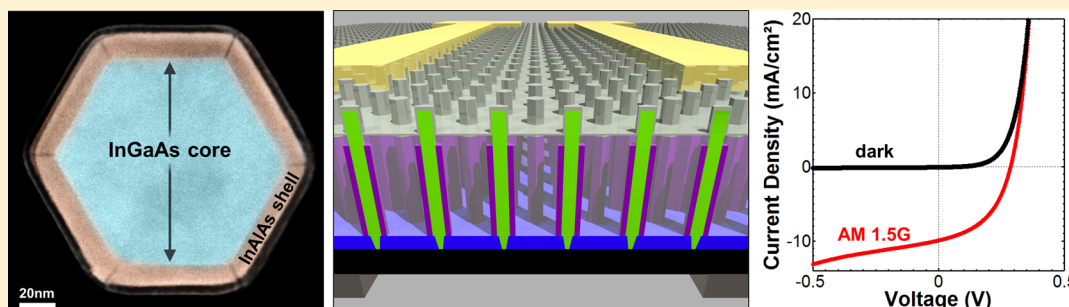
ABSTRACT: Core–shell nanowires (NW) have become very prominent systems for band engineered NW heterostructures that effectively suppress detrimental surface states and improve performance of related devices. This concept is particularly attractive for material systems with high intrinsic surface state densities, such as the low-bandgap In-containing group-III arsenides, however selection of inappropriate, lattice-mismatched shell materials have frequently caused undesired strain accumulation, defect formation, and modifications of the electronic band structure. Here, we demonstrate the realization of closely lattice-matched radial InGaAs–InAlAs core–shell NWs tunable over large compositional ranges $[x(Ga){\sim}y(Al) = 0.2{-}0.65]$ via completely catalyst-free selective-area molecular beam epitaxy. On the basis of high-resolution X-ray reciprocal space maps the strain in the NW core is found to be insignificant ($\varepsilon < 0.1\%$), which is further reflected by the absence of strain-induced spectral shifts in luminescence spectra and nearly unmodified band structure. Remarkably, the lattice-matched InAlAs shell strongly enhances the optical efficiency by up to 2 orders of magnitude, where the efficiency enhancement scales directly with increasing band offset as both Ga- and Al-contents increase. Ultimately, we fabricated vertical InGaAs–InAlAs NW/Si photovoltaic cells and show that the enhanced internal quantum efficiency is directly translated to an energy conversion efficiency that is ∼3−4 times larger as compared to an unpassivated cell. These results highlight the promising performance of lattice-matched III−V core–shell NW heterostructures with significant impact on future development of related nanophotonic and electronic devices.

KEYWORDS: *InGaAs nanowires, HRXRD, photoluminescence, strain, energy conversion efficiency, catalyst-free selective area growth*

InGaAs-based nanowires (NW) comprise one of the technologically most relevant nanoscale semiconductor systems, owing to the multitude of their unique properties. Intrinsically, they offer band gap and emission wavelength tuning capabilities over wide spectral ranges in the infrared (IR, ∼880−3500 nm), high saturation velocities and electron mobilities, tunable Schottky barrier heights, large absorption coefficients, and significantly alleviated lattice mismatch restrictions due to their inherently one-dimensional (1D) structural nature.[1] This fueled not only recent epitaxial integration efforts on silicon (Si)

platform[2−5] but also development of high-performance nanophotonic and electronic devices. Various integrated InGaAs NW-based devices have thus emerged, such as nanolasers,[6] photonic crystal lasers,[7] light-emitting diodes (LED),[8] and solar cells,[3,9] as well as tunnel diodes,[10] short-channel 3D transistors[11] beyond
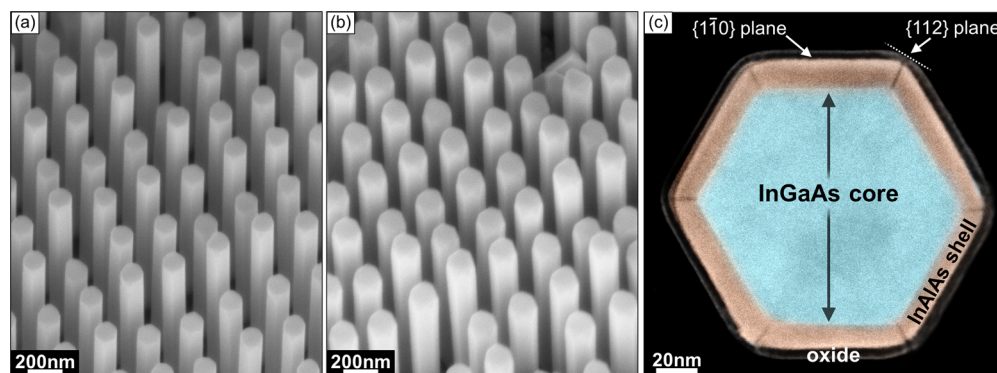
Figure 1. SEM images of (a) InGaAs NW array with a nominal Ga-content of $x(\text{Ga}) = 0.47$ and (b) capped with an InAlAs shell with the same nominal Al-content; (c) color-coded STEM-HAADF cross-sectional image of the core−shell heterostructure prepared from the same sample, exhibiting a ∼11 nm-thick InAlAs shell and a ∼5 nm-thick amorphous oxide layer on top.

the 10 nm technology node,[12] and efficient terahertz (THz) emitters.[13]

Despite these promising advances, a major limitation of the high surface-to-volume NWs is their susceptibility to detrimental surface states under ambient conditions. These surface states lead to a modification of the electronic band structure in the vicinity of the InGaAs surface, which depends strongly on their density but also on composition. As known from studies of planar InGaAs, high surface state densities cause either surface Fermi level pinning above the conduction band minimum (CBM) (case of In-rich InGaAs) or pinning of the Fermi level in the middle of the band gap (case of Ga-rich InGaAs), leading to downward/upward bending and surface electron accumulation/depletion, respectively.[14,15] The non-flat band conditions and charge carrier redistribution thus strongly inhibit the performance of optical and electrical NW device structures.

For example, high surface recombination velocities and nonradiative recombination due to surface states[16,17] strongly degrade the internal quantum efficiency (IQE) of InGaAs NWs in the entire compositional range. This critically limits observation of efficient luminescence only to low temperatures and large-diameter NW structures.[18−22] The high surface recombination velocities in (In,Ga)As-based materials have naturally also led to inferior performance of NW-based photovoltaic cells as compared to planar counterparts.[23] Surface states in thin III−V NWs also dominate the electrical transport properties, inducing large surface sheet densities that degrade electron mobility via surface scattering, as in for example, InAs NWs.[24,25] Also, they are responsible for increased interface state defect densities (D_{it}) in InGaAs-NW metal-oxide-semiconductor field effect transistors[12,26] and they even cause amphoteric conductivity behavior as in, for example, GaAs NWs.[27] The impaired electron mobilities in as-grown, unpassivated In(Ga)As NWs are further considered to pose intrinsic limits to photoconductivity and terahertz emission efficiency.[13]

Passivation of the surface states on InGaAs-based NWs is therefore of utmost importance to improve the optical and electrical properties of NW-based devices. While there has been substantial work on surface passivation of binary InAs and GaAs NWs to produce core−shell NWs, much less efforts have been dedicated to the development of core−shell NW heterostructures suitable for ternary InGaAs NWs. In the case of binary InAs NWs, common surface passivating layers include In(As)P[28−31] and Ga(In)As[32,33] shells, however, their relatively large lattice-mismatch to InAs [i.e., up to 3.1% in In(As)P and 7% in Ga(In)As], lead to substantial strain, defect formation, and

modifications of the electronic band structure of the NW core.[29,31,32] For binary GaAs NWs, various different mismatched shell material systems were investigated (i.e., GaP, GaAsP, and GaInP), though AlGaAs shells seem most appropriate due to their superior lattice matching properties. Core−shell GaAs-AlGaAs NWs have thus enabled very high optical efficiency with increased carrier lifetime and charge carrier mobility,[21,34,35] promoting the performance of high-efficiency photonic and high-speed optoelectronic NW-based devices.[36−39]

For ternary InGaAs NWs, the majority of the few studies performed so far exploited GaAs passivating layers. These are, however, prone to mismatch-related defect formation at the InGaAs−GaAs core−shell interface[40] yielding low quantum efficiencies.[6,22] As an alternative, H. Sun et al. recently demonstrated increased carrier lifetime and quantum efficiency of ∼0.6−0.9 μm wide $\text{In}_{0.12}\text{Ga}_{0.88}\text{As}$ micropillars by use of an InGaP shell layer.[22] Furthermore, selectively doped InP/$\text{In}_{0.5}\text{Al}_{0.5}\text{As}$ passivating layers have been employed on $\text{In}_{0.7}\text{Ga}_{0.3}\text{As}$ NW channels for vertical NW transistors on Si.[11] Indeed, the use of InAlAs passivating layers on InGaAs NWs is extremely appealing. This is because (i) InAlAs is commonly used as a barrier in the important $\text{In}_{0.53}\text{Ga}_{0.47}\text{As}/\text{In}_{0.52}\text{Al}_{0.48}\text{As}$ heterostructure system lattice-matched to InP for planar high-speed electronic and optoelectronic devices,[41,42] and (ii) unlike InGaP it enables complete lattice-matching to InGaAs over nearly the entire compositional range.

Here, we systematically investigate the catalyst-free growth and properties of completely lattice-matched radial InGaAs−InAlAs core−shell NWs over large compositional ranges [$x(\text{Ga})$, $y(\text{Al}) \sim 0.2−0.65$]. High-resolution X-ray diffraction (HRXRD) and complementary transmission electron microscopy (TEM) investigations reveal overall insignificant strain at the core−shell heterointerfaces. The InAlAs shell is shown to serve as a very effective surface passivating layer that strongly enhances the optical efficiency. Ultimately, we demonstrate a vertical InAlAs-InGaAs NW/Si photovoltaic cell with an efficiency ∼3−4 times larger as compared to an unpassivated cell, highlighting the significantly suppressed surface recombination and improved charge carrier conductivity by the InAlAs shell.

All InGaAs−InAlAs core−shell NWs were grown on slightly p-type (boron-doped) Si (111) substrates (1−30 Ωcm) by solid-source molecular beam epitaxy (MBE) in an entirely catalyst-free growth regime.[1] To guarantee highest possible uniformity in NW morphology and composition, growth was performed on specific SiO$_2$ mask templates. These contain ∼1 × 1 cm^2 large periodic arrays of mask openings (80 nm diameter) with pitch of 250 nm,

as prepatterned by nanoimprint lithography (NIL).[4,31] First, the growth of the $In_{1−x}Ga_xAs$ NW cores was initiated for 1 h at a temperature of 560 °C for low Ga-content InGaAs NWs (x(Ga) < 0.4) and 570 °C for high Ga-content InGaAs NWs (x(Ga) > 0.4), respectively. For all growths, the total group-III flux was fixed at 0.36 Å/s, while the Ga-flux was adjusted to yield systematic variation of the nominal Ga-content [x(Ga) ∼ 0.2− 0.6] under otherwise constant As_4 beam equivalent pressure (BEP = 3.5 × 10$^{−5}$ mbar). Note that under these growth conditions, the catalyst-free growth yields excellent compositional homogeneity along single NWs and across entire NW arrays.[1,4] After the core growth, the shutters of the group-III elemental sources were closed for 2 min while the temperature was ramped down to 510 °C before $In_{1−y}Al_yAs$ shell growth resumed for another 30 min. For each sample, the Al-content y(Al) of the shell was adjusted to the same value as the Ga-content x(Ga) of the core [x(Ga) = y(Al)] to obtain close lattice matching conditions. In the following, we will refer to such structures with identical composition between core and shell simply as x(Ga)/y(Al). All other growth fluxes during shell growth, such as the As_4-BEP and In-flux, were identical to the respective fluxes used for core growth. In order to assess the specific properties of the core−shell NWs, core-only (InGaAs) NW reference samples were also grown for comparison.

Figure 1 shows exemplary scanning electron microscopy (SEM) images of the NW arrays grown with x(Ga)/(Al) = 0.47, where (a) refers to the "core-only" structure and (b) to the core− shell structure containing the radial InAlAs passivation layer. The images show excellent high-periodicity arrays with homogeneous size distribution and growth yields (NW per predefined nucleation site) of >90%. This is found for all investigated NW samples which further exhibit very similar sizes (lengths of ∼0.6− 0.8 μm, diameters of ∼120−140 nm). Only one sample [x(Ga)/ y(Al) = 0.35] shows slightly larger diameter (shell thickness) and a total length that is significantly larger than the respective NW core (see Supporting Information, Figure S1). Furthermore, all NW arrays are vertically well aligned along the [111] direction and the major sidewall surfaces correspond to the {1$\bar{1}$0} family of planes, as verified by TEM measurements.[19]

To closely examine the geometrical shape and size, as well as the compositional contrast of the InGaAs−InAlAs core−shell NW heterostructure, we prepared focused ion beam (FIB)-cut cross-sectional lamellas. Details regarding FIB-based specimen preparation can be found elsewhere.[21,31] A typical cross-sectional view as recorded by a FEI-Titan 80-300 along the [111] zone axis of a single NW in scanning-TEM/high angle annular dark field (HAADF) mode is shown in Figure 1(c). The ∼120 nm thick hexagonal InGaAs core with {1$\bar{1}$0} side facets is conformally surrounded by a homogeneous ∼11 nm thick InAlAs shell as well as a ∼5 nm thick oxide layer on top. The formation of the thin oxide layer is attributed to the partial oxidation of the InAlAs layer after transfer to ambient environment. In addition, the shell exhibits six dark contrast stripes that propagate from the corner regions of adjacent {1$\bar{1}$0} sidewall facets of the core all the way to the surface of the shell. The volume of these regions was too low to yield sufficient signal intensity in associated energy-dispersive X-ray spectroscopy (EDXS) measurements. However, we anticipate that they correspond to regions of Al-enrichment, as previously identified in ref 11 and as also expected from the Z-contrast intensity ratios in the STEM/HAADF image. We note that such segregation effect is commonly observed in Al-containing shells of typical III−V semiconductor core−shell NWs (e.g., GaAs−AlGaAs, GaAs−AlInP, and so forth[21,43]),

which arises from the formation of {112}-oriented nanofacets during shell growth.[21] Overall, the microstructure of the InGaAs−InAlAs core−shell NWs exhibits the common disordered layer stacking of catalyst-free grown InGaAs NWs as well as inclusions of wurtzite (WZ) segments when the InGaAs composition is tuned across the In-rich side[19] (not shown). This is expected based on the common crystal structure transfer mechanisms observed in III−V core−shell NW heterostructures.[21,31,44]

Further insights into the microstructure, strain, as well as the actual composition of the as-grown InGaAs−InAlAs core−shell NWs were obtained by high-resolution XRD. For this, reciprocal space maps (RSM) were taken using a laboratory diffractometer with a Cu K α source for radiation, where the sample was aligned such that the Q_z axis is parallel to the [111] growth axis of the NW array. RSMs were recorded around the symmetric (333)$_{ZB}$, and asymmetric (513)$_{ZB}$, (224)$_{ZB}$, and (205)$_{WZ}$ reflections (the subscripts denote Bragg reflections of the ZB and WZ lattices, respectively).

The (333)$_{ZB}$ and (513)$_{ZB}$ Bragg peaks correspond to (006)$_{WZ}$ and (2$\bar{1}$6)$_{WZ}$ Bragg peaks, respectively, while the (224)$_{ZB}$ has no correspondence in the WZ reciprocal space, and the (205)$_{WZ}$ Bragg peak has no ZB correspondence. A representative RSM of an InGaAs−InAlAs core−shell NW array (with nominal x(Ga)/ y(Al) = 0.6) is shown in Figure 2. From the positions of the Bragg

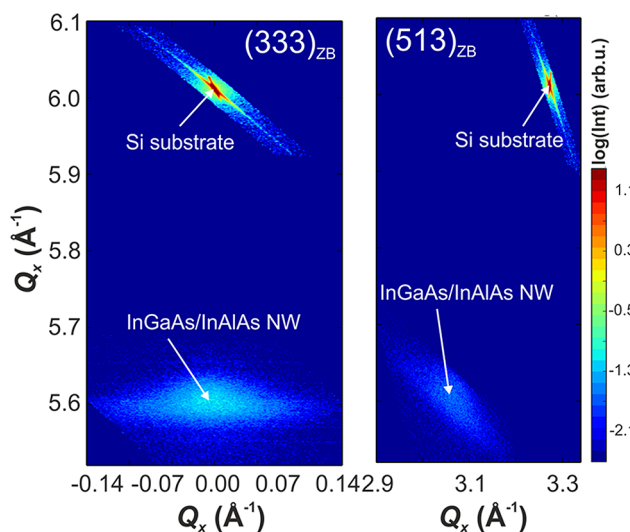**Figure 2.** Reciprocal space maps around the (333)$_{ZB}$ and (513)$_{ZB}$ Bragg reflections for the NW sample with nominal x(Ga)/y(Al) = 0.6. Peaks due to the Si substrate and the NWs are indicated, and intensities are plotted on a logarithmic scale. The broadening of the NW reflection due to a small tilt distribution of the NWs is clearly visible.

peaks in reciprocal space, we determine the lattice parameters along the NW growth direction and perpendicular to it in different azimuthal directions. In all NW samples, we see both ZB and WZ reflections, consistent with the stacking sequence observed by TEM. From the width along Q_z in the (224)$_{ZB}$ and (205)$_{WZ}$ reflections, we can further estimate the relative average lengths of WZ and ZB segments and find that the WZ segments are on average longer than the ZB ones in all samples with a trend toward longer WZ segments for smaller Ga contents. This trend agrees also favorably with recent observations by TEM.[19] We thus treat the measured lattice parameters as hexagonal a (perpendicular to growth direction) and c (along growth

Table 1. Summary of XRD-Measured Lattice Parameters (a, c Denote the Two Lattice Constants of the Wurtzite Structure), Chemical Compositions, and Strain

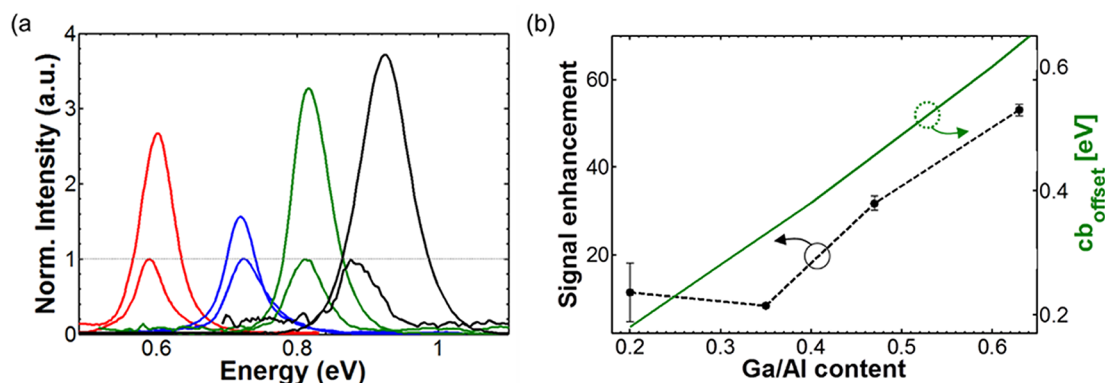| sample	NW structure	a (Å)	c (Å)	$x(Ga)_{core}$	$x(Ga)_{core-shell}$	ε_a (%)	ε_c (%)
In-rich InGaAs	InGaAs core	4.159	6.862	0.37 (±0.02)		−0.23	0.11
	InGaAs−InAlAs	4.171	6.866		0.35 (±0.07)	−0.08	0.03
midcomp. InGaAs	InGaAs core	4.143	6.812	0.46 (±0.02)		0	−0.01
	InGaAs−InAlAs	4.151	6.807		0.46 (±0.07)	0.19	−0.09
Ga-rich InGaAs	InGaAs core	4.094	6.729	0.64 (±0.02)		0.05	−0.01
	InGaAs−InAlAs	4.094	6.734		0.63 (±0.07)	−0.02	−0.01

Figure 3. (a) PL spectra of composition-tuned InGaAs (core-only) and InGaAs−InAlAs core−shell NWs recorded at 8K and excitation power of 1.1 kW/mm^2. For better comparability the PL spectra of all InGaAs (core-only) NWs are normalized. (b) PL enhancement factor (ratio of integrated PL intensity of the respective core−shell versus core-only structure) as a function of $x(Ga)/y(Al)$-content and correlated with the conduction band offset. Band offsets are derived assuming conventional bulk ZB lattice parameters.[46] Error bars stem from a statistical analysis of several measurements performed at different positions across the NW sample.

direction) unit cell sizes, and give all strains with respect to hexagonal InAs and GaAs.

In order to convert the measured lattice parameters in composition and strain values, we assume that the lattice parameters of InGaAs and InAlAs vary with composition according to Vegard's rule. For the elastic parameters, we also use a linear interpolation and values for the hexagonal lattices are converted according to ref 45. Usually, free-standing NWs are found to be elastically relaxed except for a small part close to the interface to the substrate.[57] In our case, the evaluated strains are indeed also very small, however, we still measure finite values (see Table 1). We consider two effects which may contribute to the nonzero strains: First, the slight difference in lattice parameters between WZ and ZB lead to a mutual straining of the individually stacked segments with a resulting in-plane strain (given with respect to pure WZ material) that varies with WZ/ZB ratio. Second, if the shell is not perfectly lattice-matched to the core, this will also result in a mutual strain. To estimate which contribution dominates over these relatively small finite strain values, we performed additional finite element modeling (FEM) simulations of the as-measured XRD patterns (see Supporting Information). These were necessary because the contribution of the InAlAs shell was too weak in the measured signal, due to its relatively thin layer thickness. Essentially, we found that an in-plane strain value of <0.1% in the NW core would correspond to a deviation from the exact lattice matching condition by a maximum of 7%. On the other hand, comparing the in-plane strains between core-only and core−shell NWs (Table 1), there is no direct correlation as the magnitudes of the strain values do not systematically increase upon passivation by the InAlAs shell. This suggests that the observed strain is most likely due to the mutual straining of the WZ/ZB stacking and that the lattice-

matching condition between InGaAs core and InAlAs shell is close to perfect.

To identify the beneficial effects of the InAlAs shell passivation on the optical properties we performed extensive micro-photoluminescence (μPL) studies using a home-built setup dedicated to characterization in the mid-infrared spectral range. Here, a chopped He/Ne laser (633 nm) is used to excite the NW array inside a He-flow cryostat and the resulting signal is detected via lock-in technique using a monochromator and lN$_2$-cooled InSb photodetector. The spot size of the exciting laser is adjusted to about 2 μm, equivalent to an ensemble measurement of ~50 NWs as given by the pitch of the as-grown NW arrays. Further experimental details can be found elsewhere.[19] Unless otherwise specified, the excitation power density is kept at 1.1 kW/mm^2 and the measurement temperature was at 8 K. Considering the very high and uniform growth yield of all investigated NW arrays (>90%), we can thus compare absolute PL intensities and their quantum efficiencies because the excitation volume was identical for all samples.

Figure 3a directly compares PL spectra from the InGaAs−InAlAs core−shell NW arrays with different compositions and with respect to their unpassivated "core-only" structures. Note that for better comparison we normalized the PL spectra for all core-only reference samples. Several interesting features are observed: First, the luminescence for both the core-only reference samples and core−shell NW heterostructures shifts to the blue (higher PL peak energies) as the composition is tuned from the In-rich to the Ga-rich InGaAs side. Clearly, this is expected based on the increase of band gap energy with increasing Ga content. This demonstrates that we can tune the emission wavelength of the InGaAs NWs over relatively wide ranges and, importantly, also capture the technologically relevant telecommunication band (~1.3−1.55 μm, that is, $E \sim 0.8-0.95$

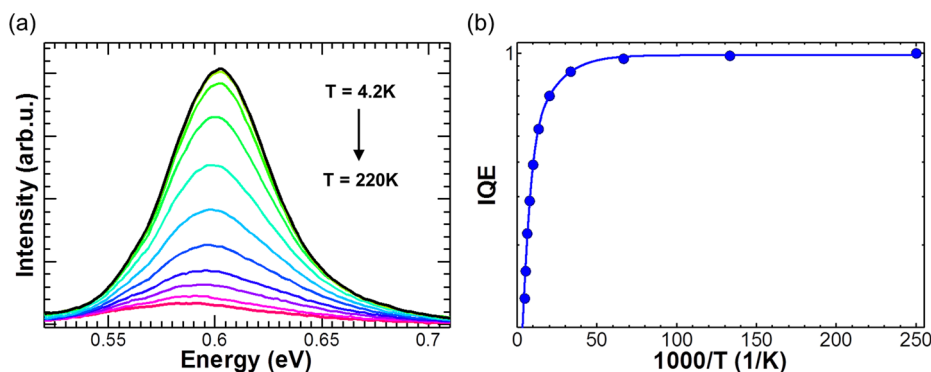**Figure 4.** (a) Representative temperature-dependent PL spectra obtained for an InGaAs−InAlAs core−shell NW sample $[x(Ga)/y(Al) = 0.2]$ at an excitation power density of 1.1 kW/mm^2. (b) Corresponding Arrhenius plot of the internal quantum efficiency (IQE), which yields an IQE of 11.3% at room temperature.

eV). Second, the PL peak positions of the core−shell NWs match closely with those of the core-only NWs, except for the sample with highest $x(Ga)/y(Al)$-content (as will be further discussed below). This demonstrates that the InGaAs NW core and InAlAs shell are closely lattice-matched with insignificant strain in line with the presented HRXRD data. Note also that the PL peakwidth of the core luminescence does not change between the core-only and the core−shell NWs, confirming the high-quality closely lattice-matched shell growth. However, the peakwidth rises with $x(Ga)/y(Al)$ content, that is, from ∼40 meV $[x(Ga)/y(Al) = 0.2]$ to ∼70 meV $[x(Ga)/y(Al) = 0.63]$, which we attribute to an increasingly larger stacking disorder of the underlying microstructure toward Ga-rich InGaAs NWs.[19]

Most importantly, the intensity of the NW core luminescence is strongly enhanced upon passivation, reflecting the anticipated suppression of surface state induced nonradiative recombination.[21,31,34] Interestingly, the PL enhancement factor (i.e., integrated PL intensity ratio between passivated and unpassivated NWs) scales directly with the increase in $x(Ga)/y(Al)$-content. While the enhancement factor is only ∼10 for the In-rich InGaAs NW arrays $[x(Ga)/y(Al) = 0.2]$ it rises to ∼50 for the Ga-rich InGaAs NWs $[x(Ga)/y(Al) = 0.63]$ (see Figure 3b). Note, the PL intensity data from the sample with $x(Ga)/y(Al) = 0.35$ deviate slightly from this trend. This can be explained by the slightly thicker shell and additional axial InAlAs top segment in these NWs (see Supporting Information), which limits the diffusion of photoexcited carriers to the NW core for radiative recombination.

Nevertheless, the overall observed scaling behavior can be explained by two main effects: One is that with increasing $x(Ga)/y(Al)$-content the band-offset of the InAlAs shell material increases steadily with respect to the band gap of the InGaAs core (see Figure 3b). Hence, carriers excited in the shell relax more efficiently into the core and the InAlAs layer acts as an increasingly efficient barrier for larger Al-content, which effectively confines carriers to the NW core. This is because increasing barrier height more strongly confines the electron wave function leading to increased luminescence efficiency, similar to recent observations in InAs−InAsP core−shell NWs.[31] For this reason also no luminescence from the InAlAs shell is observed in all spectra, as also expected from the relatively thin shell layer thicknesses. Another effect is that the reduced surface state density upon passivation reduces also the surface band-bending, thus leading to larger spatial overlap of electrons in the conduction band (CB) and holes in the valence band (VB) which increases radiative efficiency. In particular, in unpassivated

InGaAs NWs it is anticipated that increasing the Ga-content from $x(Ga)$ ∼0.2, where nearly flat-band conditions prevail,[14,15] to larger $x(Ga)$ increases the surface band bending and thus the spatial separation of charge carriers. Hence, the effect of PL enhancement due to passivation by InAlAs is expected to be higher in samples with higher Ga-content. The spatial charge carrier separation due to surface band bending may further explain the slight redshift in the PL of core-only NWs with respect to the core−shell NWs. This is expected to lead to more indirect radiative transitions at lower energy, which is most pronounced in InGaAs NW samples with compositions far away from $x(Ga) \sim 0.2$ (near-flat band conditions), particularly in the NW array with $x(Ga)/y(Al) = 0.63$ (see Figure 3a). Furthermore, we do not expect a significant influence of the stacking disorder in the InAlAs shell on the InGaAs core luminescence enhancement, since the crystal structure of the shell is a direct replica of the core structure.

To further confirm the enhanced optical efficiency we evaluated the internal quantum efficiency (IQE) of the core−shell NW heterostructures. The material-inherent IQE is an important metric to evaluate the intrinsic performance of optoelectronic devices, such as LEDs and photovoltaic cells. In general, IQE is relatively low in NW-based devices due to large surface recombination, particularly in unpassivated NWs.[22] To derive the IQE for our = InGaAs−InAlAs core−shell NWs we therefore performed temperature-dependent PL measurements, as exemplified in Figure 4a for the sample with lowest $x(Ga)/y(Al)$-content of 0.2. As expected, with increasing temperature the intensity decreases and the peak position shifts gradually to lower energies. Note, however, that the peak shift is much weaker as expected for a high-quality bulk semiconductor. This is mainly due to stacking-defect induced localized trap states in the InGaAs NWs that compete against the classical Varshni-type band shrinkage.[1,18,19]

Figure 4b depicts a $1/T$-Arrhenius plot of the corresponding IQE, which is derived from the ratio of the integrated PL intensities at temperature T and at 4 K $[IQE = I(T)/I(4 K)]$.[47] Although for this sample PL was only observed up to ∼220 K, we were able to extrapolate the IQE to room temperature. This was realized by employing the activation energy E_A for the nonradiative PL-quenching process at increased temperature that arises due to carrier escape from the InGaAs core to the InAlAs barrier. A best fit to the data yielded $E_A = 25$ meV, which further results in an IQE of 11.3% at room temperature for this InGaAs−InAlAs core−shell NW sample. Although this value is still comparatively low with respect to typical IQE in planar
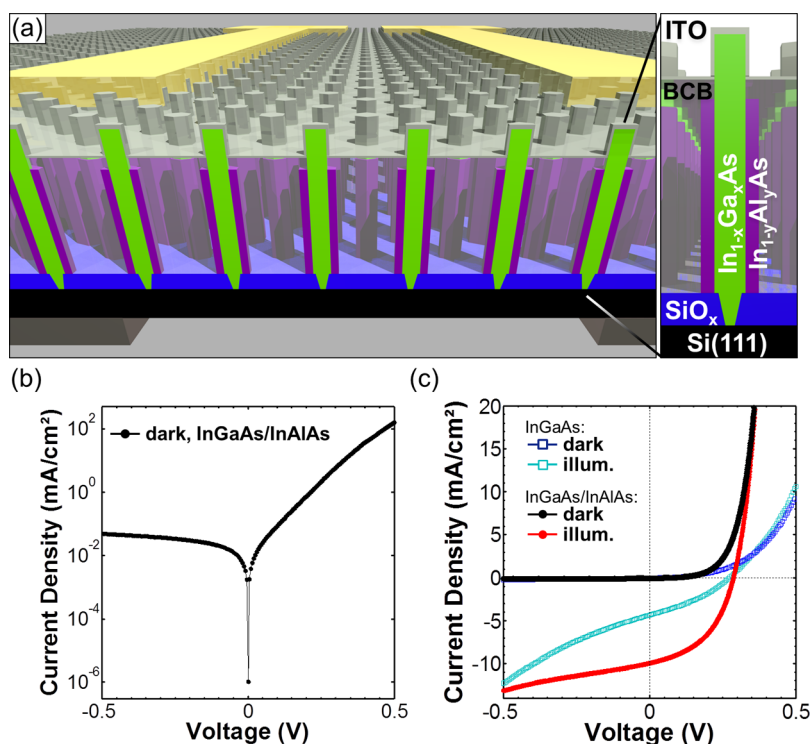
Figure 5. (a) Schematic illustration of the vertical InGaAs-NW based PV cell structure on Si substrate. (b,c) Typical $I-V$ diode characteristics at room temperature as obtained for the passivated core–shell NW array in comparison to the unpassivated core-only array. Data are recorded in dark and under illumination using a tungsten–halogen source with AM 1.5G and input power of 1000 W/m^2.

InGaAs-based heterostructures,[48] it compares favorably to some of the best IQE values reported for InGaAs NWs so far and is significantly better than, for example, unpassivated, GaAs- or AlGaAs-passivated InGaAs NWs.[22] This directly demonstrates the beneficial effect of the lattice-matched InAlAs passivating shell, making these structures viable for performance tests in nanostructured optoelectronic devices.

Hence, the distinct functionality of the InAlAs surface passivation layer is ultimately tested in InGaAs NW photovoltaic (PV) cells and affirmed by enhancements in photoconductivity and PV cell performance. In fact, this needs to be expected because high IQE translates to more efficient energy conversion in a PV cell, particularly because suppression of nonradiative surface recombination increases the fill factor.[49,50] To demonstrate this we fabricated vertical NW photodiodes directly from the as-grown free-standing NW arrays on Si (111), where the intrinsically n-InGaAs (undoped)/p-Si heterointerface serves as an axial p–n junction. It should be noted though that, in general, axially arranged NW p–n junctions are considered less efficient over radially arranged p-n core–shell NW photodiode structures because of higher surface recombination rates and inferior minority carrier collection.[50,51] Nevertheless, axial NW-based p-n heterojunctions provide still an important testbed to investigate the role of surface recombination and photoconductivity in PV cells, as has been illustrated in various heteroepitaxial NW-based photodiodes, for example, n-InAs NW/p-Si,[52] p-GaN NW/n-Si,[53] and so forth.

To fabricate PV cells the NW arrays were embedded in thick insulating benzocyclobutene (BCB) polymer, which was subsequently etched by O$_2$/SF$_6$-based reactive ion etching to expose the tips of the NWs. Mesa structures (180 μm × 300 μm) were then realized using optical lithography. After development and O$_2$ plasma treatment the InAlAs shell of the protruding NWs

was selectively etched in HCl/H$_2$O (3:1) to access the InGaAs core and ensure good ohmic contacts. As such, sputter-deposited 100 nm thick indium tin oxide (ITO) was used that was further annealed under ambient conditions (300 °C, 60 min) to obtain high transparency and conductivity. Finally, 100 nm thick feed-lines were defined to the perimeter of the top contacts to enable wire bonding, while 100 nm/50 nm Ag/Au electrodes were used as back contacts on the backside of the p-type Si (111) substrate. Figure 5a shows a schematic of the final device, which contains about ~4 × 10^5 NWs assuming a NW growth yield of ~90%. The current–voltage ($I-V$) characteristics of wire-bonded devices were then recorded at room temperature by a current–voltage sourcemeter (Keithley 2400) in dark and under illumination using a calibrated tungsten-halogen lamp to achieve equivalent air mass 1.5 global conditions (AM1.5G, 1000W/m^2).

Figure 5b,c displays the $I-V$ characteristics in dark and under illumination for the as-fabricated InGaAs–InAlAs core–shell NW-based PV cell [x(Ga)/y(Al) = 0.47]. In dark, a typical diode behavior is obtained with a rectification ratio of ~10^3 at ±0.5 V and a very low reverse bias leakage current (1.5 × 10^{-9} A at −0.5 V), indicating a high-quality p–n junction with efficient isolation between top and bottom contacts. The diode ideality factor is ~2.5 as extracted from the semilogarithmic plot of the $I-V$ data (see Figure 5b). These diode parameters are very similar to those reported earlier for n-In(Ga)As-NW/p-Si heterojunction diodes.[3,10,54] Under illumination a clear photoresponse is observed with a photocurrent that is >10^3-times larger than the dark current at small reverse bias.

Note that the finite slope in the $I-V$ curve under reverse bias indicates a non-negligible shunt resistance (~0.6 MΩ), which is expected to obscure the ideality factor. From the photoresponse data we further extracted a short-circuit current density (I_{SC}) of 10 mA/cm^2 and an open-circuit voltage (V_{OC}) of 0.29 V,

respectively (see also Table 1). The fill factor (FF = $I_{max}V_{max}/I_{SC}V_{OC}$) is 0.46, resulting in an energy conversion efficiency (ECE) of 1.3% (ECE = $I_{max}V_{max}$FF/P_{in}), where I_{max} and V_{max} are the current and voltage at maximum power points in the $I-V$ curve. Note that for the calculations of the current density we took the total contact area (i.e., equivalent substrate area) into account, because for the low p-type doping of the Si substrate the depletion region in the Si extends further than the distance between neighboring NWs. We also measured the external quantum efficiency (EQE) of this device, which resulted in a maximum EQE of ~15% at ~900−1000 nm (see Supporting Information).

For comparison, Figure 5c illustrates also the $I-V$ diode characteristics of an identical device fabricated from the equivalent InGaAs NW array [x(Ga) = 0.46] without InAlAs passivation. Obviously, the performance of the unpassivated NW array is significantly inferior with lower I_{SC} and FF and a conversion efficiency that is ~3× lower than the passivated InGaAs NW array device (see Table 2). In addition, the $I-V$

Table 2. Comparison of Photovoltaic Device Metrics for Unpassivated (InGaAs-only) and Surface Passivated (InGaAs−InAlAs Core−Shell) NW Arrays

NW structure	I_{SC} (mA/cm^2)	V_{OC}(V)	P_{max} (μW)	FF	ECE (%)
InGaAs only	4.3	0.28	0.12	0.34	0.4
InGaAs−InAlAs	10	0.29	0.40	0.46	1.3

characteristic of the unpassivated device exhibits a distinct "S-shape" behavior. This is commonly attributed to interfacial effects at the NW surface (dipoles, defects, etc.), creating barriers for carrier extraction that are further responsible for losses in I_{SC} and FF.[55−57] Thus, the absence of the S-shape $I-V$ characteristic reflects directly the superior photoconductivity and performance of the passivated device. Overall, these characteristics suggest that in the axial heterojunction geometry the passivated InAlAs-InGaAs core−shell NW structure acts as a low-loss carrier conductor and that most of the photocarriers are generated in the Si substrate.[58] This is further supported by measurements of the wavelength-dependent external quantum efficiency which indicate that that photocarrier generation by the NWs is negligible (see Supporting Information).

In conclusion, we investigated catalyst-free growth of high-uniformity lattice-matched InGaAs−InAlAs core−shell NW arrays on Si over wide compositional ranges. The close lattice-matching behavior with insignificant heteroepitaxial strain between core and shell was verified based on HRXRD and TEM analysis. The InAlAs shell passivation is demonstrated to significantly enhance radiative recombination resulting in internal quantum efficiencies of IQE > 10% without inducing shifts in the transition energies as often observed in lattice-mismatched core−shell NW systems. We further confirmed the beneficial InAlAs passivation layer via increased photovoltaic (PV) conversion efficiencies that are ~3−4 times higher than in state-of-the-art unpassivated InGaAs-NW based PV cells. These findings open important perspectives for efficient InGaAs core−shell NW-heterojunction devices that are strain-free and tunable over wide spectral ranges.

■ ASSOCIATED CONTENT

ⓢ Supporting Information
Detailed information on morphological investigations, finite element modeling, and photoresponse. The Supporting Information is available free of charge on the ACS Publications website at DOI: 10.1021/acs.nanolett.5b00979.

■ AUTHOR INFORMATION

Corresponding Authors
*E-mail: Julian.Treu@wsi.tum.de.
*E-mail: Gregor.Koblmueller@wsi.tum.de.

Notes
The authors declare no competing financial interest.

■ REFERENCES
(1) Koblmüller, G.; Abstreiter, G. *Phys. Status Solidi RRL* **2014**, 8, 11.
(2) Tomioka, K.; Tanaka, T.; Hara, S.; Hiruma, K.; Fukui, T. *IEEE J. Sel. Top. Quantum Electron.* **2011**, 17, 1112.
(3) Shin, J. C.; Kim, K. H.; Yu, K. J.; Hu, H.; Yin, L.; Ning, C.-Z.; Rogers, J. A.; Zuo, J.-M.; Li, X. *Nano Lett.* **2011**, 11, 4831.
(4) Hertenberger, S.; Funk, S.; Vizbaras, K.; Yadav, A.; Rudolph, D.; Becker, J.; Bolte, S.; Döblinger, M.; Bichler, M.; Scarpa, G.; Lugli, P.; Zardo, I.; Finley, J. J.; Amann, M.-C.; Abstreiter, G.; Koblmüller, G. *Appl. Phys. Lett.* **2012**, 101, 043116.
(5) Hou, J. J.; Han, N.; Wang, F.; Xiu, F.; Yip, S. P.; Hui, A. T.; Hung, T. F.; Ho, J. C. *ACS Nano* **2012**, 12, 3624.
(6) Chen, R.; Tran, T.-T. D.; Ng, K. W.; Ko, W. S.; Chuang, L. C.; Sedgwick, F. G.; Chang-Hasnain, C. *Nat. Photonics* **2011**, 5, 170.
(7) Scofield, A. C.; Kim, S.-H.; Shapiro, J. N.; Lin, A.; Liang, B.; Scherer, A.; Huffaker, D. L. *Nano Lett.* **2011**, 11, 5387.
(8) Dimakis, E.; Jahn, U.; Ramsteiner, M.; Tahraoui, A.; Grandal, J.; Kong, X.; Marquart, O.; Trampert, A.; Riechert, H.; Geelhaar, L. *Nano Lett.* **2014**, 14, 2604.
(9) Shin, J. C.; Mohseni, P. K.; Yu, K. J.; Tomasulo, S.; Montgomery, K. H.; Lee, M. L.; Rogers, J. A.; Li, X. *ACS Nano* **2012**, 6, 11074.
(10) Yang, T.; Hertenberger, S.; Morkötter, S.; Abstreiter, G.; Koblmüller, G. *Appl. Phys. Lett.* **2012**, 101, 233102.
(11) Tomioka, K.; Yoshimura, M.; Fukui, T. *Nature* **2012**, 488, 189.
(12) Si, M.; Gu, J. J.; Wang, X.; Shao, J.; Li, X.; Manfra, M. J.; Gordon, R. G.; Ye, P. *Appl. Phys. Lett.* **2013**, 102, 093505.
(13) Arlauskas, A.; Treu, J.; Saller, K.; Beleckaite, I.; Koblmüller, G.; Krotkus, A. *Nano Lett.* **2014**, 14, 1508.
(14) Kajiyama, K.; Mizushima, Y.; Sakata, S. *Appl. Phys. Lett.* **1973**, 23, 458.
(15) Lüth, H. *Phys. Status Solidi A* **2001**, 187, 33.
(16) Aspnes, D. *Surf. Sci.* **1983**, 132, 406.
(17) Joyce, H. J.; Docherty, C. J.; Gao, Q.; Tan, H. H.; Jagadish, C.; Lloyd-Hughes, J.; Herz, L. M.; Johnston, M. B. *Nanotechnology* **2013**, 24, 214006.
(18) Koblmüller, G.; Vizbaras, K.; Hertenberger, S.; Bolte, S.; Rudolph, D.; Becker, J.; Döblinger, M.; Amann, M.-C.; Finley, J. J.; Abstreiter, G. *Appl. Phys. Lett.* **2012**, 101, 053103.
(19) Morkötter, S.; Funk, S.; Liang, M.; Döblinger, M.; Hertenberger, S.; Treu, J.; Rudolph, D.; Yadav, A.; Becker, J.; Bichler, M.; Scarpa, G.; Lugli, P.; Zardo, I.; Finley, J. J.; Abstreiter, G.; Koblmüller, G. *Phys. Rev. B* **2013**, 87, 205303.
(20) Demichel, O.; Heiss, M.; Bleuse, J.; Mariette, H.; Fontcuberta i Morral, A. *Appl. Phys. Lett.* **2010**, 97, 201907.
(21) Rudolph, D.; Funk, S.; Döblinger, M.; Morkötter, S.; Hertenberger, S.; Schweickert, L.; Becker, J.; Matich, S.; Bichler, M.;

Spirkouoska, D.; Zardo, I.; Finley, J. J.; Abstreiter, G.; Koblmüller, G. *Nano Lett.* **2013**, *13*, 1522.

(22) Sun, H.; Ren, F.; Ng, K. W.; Tran, T. T. D.; Li, K.; Chang-Hasnain, C. *ACS Nano* **2014**, *8*, 6833.

(23) Liang, D.; Kang, Y.; Huo, Y.; Chen, Y.; Cui, Y.; Harris, J. S. *Nano Lett.* **2013**, *13*, 4850.

(24) Dayeh, S. A.; Yu, E. T.; Wang, D. *Small* **2009**, *5*, 77−81.

(25) Ford, A. C.; Ho, J. C.; Chueh, Y.-L.; Tseng, Y.-C.; Fan, Z.; Guo, J.; Bokor, J.; Javey, A. *Nano Lett.* **2009**, *9*, 360−365.

(26) Connor, E. O.; Brennan, B.; Djara, V.; Cherkaoui, K.; Monaghan, S.; Newcomb, S. B.; Contreras, R.; Milojevic, M.; Hughes, G.; Pemble, M. E.; Wallace, R. M.; Hurley, P. K. *J. Appl. Phys.* **2011**, *109*, 024101.

(27) Han, N.; Wang, F.; Hou, J. J.; Xiu, F.; Yip, S.-P.; Hiu, A. T.; Hung, T. F.; Ho, J. C. *ACS Nano* **2012**, *6*, 4428.

(28) Jiang, X.; Xiong, Q.; Nam, S.; Qian, F.; Li, Y.; Lieber, C. M. *Nano Lett.* **2007**, *7*, 3214.

(29) Keplinger, M.; Martensson, T.; Stangl, J.; Wintersberger, E.; Mandl, B.; Kriegner, D.; Holy, V.; Bauer, G.; Deppert, K.; Samuelson, L. *Nano Lett.* **2009**, *9*, 1877.

(30) Lin, A.; Shapiro, J. N.; Scofield, A. C.; Liang, B. L.; Huffaker, D. L. *Appl. Phys. Lett.* **2013**, *102*, 053115.

(31) Treu, J.; Bormann, M.; Schmeiduch, H.; Döblinger, M.; Morkötter, S.; Matich, S.; Wiecha, P.; Saller, K.; Mayer, B.; Bichler, M.; Amann, M.-C.; Finley, J. J.; Abstreiter, G.; Koblmüller, G. *Nano Lett.* **2013**, *13*, 6070.

(32) Popovitz-Biro, R.; Kretinin, A.; von Huth, P.; Shtrikman, H. *Cryst. Growth Des.* **2011**, *11*, 3858.

(33) Kavanagh, K. L.; Saveliev, I.; Blumin, M.; Swadener, G.; Ruda, H. E. *J. Appl. Phys.* **2012**, *111*, 044301.

(34) Titova, L. V.; Hoang, T. B.; Jackson, H. E.; Smith, L. M.; Yarrison-Rice, J. M.; Kim, Y.; Joyce, H. J.; Tan, H. H.; Jagadish, C. *Appl. Phys. Lett.* **2006**, *89*, 173126.

(35) Parkinson, P.; Joyce, H. J.; Gao, Q.; Tan, H. H.; Zhang, X.; Zou, J.; Jagadish, C.; Herz, L. M.; Johnston, M. B. *Nano Lett.* **2009**, *9*, 3349.

(36) Tomioka, K.; Motohisa, J.; Hara, S.; Hiruma, K.; Fukui, T. *Nano Lett.* **2010**, *10*, 1639.

(37) Gallo, E. M.; Chen, G.; Currie, M.; McGucking, T.; Prete, P.; Lovergine, N.; Nabet, B.; Spanier, J. E. *Appl. Phys. Lett.* **2011**, *98*, 24113.

(38) Saxena, D.; Mokkapati, S.; Parkinson, P.; Jiang, N.; Gao, Q.; Tan, H. H.; Jagadish, C. *Nat. Photonics* **2013**, *7*, 963.

(39) Mayer, B.; Rudolph, D.; Schnell, J.; Morkötter, S.; Winnerl, J.; Treu, J.; Müller, K.; Bracher, G.; Abstreiter, G.; Koblmüller, G.; Finley, J. J. *Nat. Commun.* **2013**, *4*, 2931.

(40) Jabeen, F.; Grillo, V.; Martinelli, F.; Rubini, S. *IEEE J. Sel. Top. Quantum Electron.* **2011**, *17*, 794.

(41) Yamashita, Y.; Endoh, A.; Shinohara, K.; Higashiwaki, M.; Hikosaka, K.; Mimura, T.; Hiyamizu, S.; Matsui, T. *IEEE Electron Device Lett.* **2001**, *22*, 367.

(42) Lenox, C.; Nie, H.; Yuan, P.; Kinsey, G.; Homles, A. L.; Streetman, B. G.; Campbell, J. C. *IEEE Photonics Technol. Lett.* **1999**, *11*, 1162.

(43) Sköld, N.; Wagner, J. B.; Karlsson, G.; Hernan, T.; Seifert, W.; Pistol, M.-E.; Samuelson, L. *Nano Lett.* **2006**, *6*, 2743.

(44) Algra, R. E.; Hocevar, M.; Verheijen, M. A.; Zardo, I.; Immink, G. G. W.; van Enckevort, W. J. P.; Abstreiter, G.; Kouwenhoven, L. P.; Vlieg, E.; Bakkers, E. P. A. M. *Nano Lett.* **2011**, *11*, 1690.

(45) Martin, R. M. *Phys. Rev. B* **1972**, *6*, 4546−4553.

(46) Vurgaftman, I.; Meyer, J. R.; Ram-Mohan, L. R. *J. Appl. Phys.* **2001**, *89*, 5815.

(47) Watanabe, S.; Yamada, N.; Nagashima, M.; Ueki, Y.; Sasaki, C.; Yamada, Y.; Taguchi, T.; Tadatomo, K.; Okagawa, H.; Kudo, H. *Appl. Phys. Lett.* **2003**, *83*, 4906.

(48) Sung, L. W.; Lin, H. H. *Appl. Phys. Lett.* **2003**, *83*, 1107.

(49) Miller, O. D.; Yablonovitch, E.; Kurtz, S. R. *IEEE J. Photovoltaics* **2012**, *2*, 303.

(50) Garnett, E. C.; Brongersma, M. L.; Cui, Y.; McGehee, M. D. *Annu. Rev. Mater. Res.* **2011**, *41*, 269.

(51) Yu, S.; Roemer, F.; Witzigmann, B. *J. Photonics Energy* **2012**, *2*, 028002.

(52) Wei, W.; Bao, X. Y.; Soci, C.; Ding, Y.; Wang, Z. L.; Wang, D. *Nano Lett.* **2009**, *9*, 2926.

(53) Tang, Y. B.; Chen, Z. H.; Song, H. S.; Lee, C. S.; Cong, H. T.; Cheng, H. M.; Zhang, W. J.; Bello, I.; Lee, S. T. *Nano Lett.* **2008**, *8*, 4191.

(54) Björk, M. T.; Schmid, H.; Bessire, C. D.; Moselund, K. E.; Ghoneim, H.; Karg, S.; Lörtscher, E.; Riel, H. *Appl. Phys. Lett.* **2010**, *97*, 163501.

(55) Kumar, A.; Sista, S.; Yang, Y. *J. Appl. Phys.* **2009**, *105*, 094512.

(56) Mariani, G.; Scofield, A. C.; Hung, C.-H.; Huffaker, D. L. *Nat. Commun.* **2013**, *6*, 2509.

(57) Huang, W. J.; Sun, R.; Tao, J.; Menard, L. D.; Nuzzo, R. G.; Zuo, J. M. *Nat. Mater.* **2008**, *7*, 308−313.

(58) Mallorqui, A. D.; Alarcon-Llado, E.; Russo-Averchi, E.; Tütüncüoglu, G.; Matteini, F.; Rüffer, D.; Fontcuberta i Morral, A. *J. Phys. D* **2014**, *47*, 394017.